PCCP

PAPER

View Article Online
View Journal | View Issue

Cite this: *Phys. Chem. Chem. Phys.*, 2021, **23**, 4394

Shock wave and modelling study of the dissociation kinetics of C_2F_5I†

C. J. Cobos,[a] L. Sölter,[b] E. Tellbach[b] and J. Troe *[bc]

Received 11th December 2020,
Accepted 4th February 2021

DOI: 10.1039/d0cp06414a

rsc.li/pccp

The thermal dissociation of C_2F_5I was studied in shock waves monitoring UV absorption signals from the reactant C_2F_5I and later formed reaction products such as CF, CF_2, and C_2F_4. Temperatures of 950–1500 K, bath gas concentrations of [Ar] = 3×10^{-5}–2×10^{-4} mol cm^{-3}, and reactant concentrations of 100–500 ppm C_2F_5I in Ar were employed. Absorption-time profiles were recorded at selected wavelengths in the range 200–280 nm. It was found that the dissociation of $C_2F_5I \rightarrow C_2F_5 + I$ was followed by the dissociation $C_2F_5 \rightarrow CF_2 + CF_3$, before the dimerization reactions $2CF_2 \rightarrow C_2F_4$ and $2CF_3 \rightarrow C_2F_6$ and a reaction $CF_2 + CF_3 \rightarrow CF + CF_4$ set in. The combination of iodine atoms with C_2F_5 and CF_3 had also to be considered. The rate constant of the primary dissociation of C_2F_5I was analyzed in the framework of statistical unimolecular rate theory accompanied by a quantum-chemical characterization of molecular parameters. Rates of secondary reactions were modelled as well. Experimental rate constants for the dissociations of C_2F_5I and C_2F_5 agreed well with the modelling results. The comparably slow dimerization $2CF_2 \rightarrow C_2F_4$ could be followed both by monitoring reactant CF_2 and product C_2F_4 absorption signals, while CF_3 dimerization was too fast to be detected. A competition between the dimerization reactions of CF_2 and CF_3, the recombination of CF_2 and CF_3 forming C_2F_5, and CF-forming processes like $CF_2 + CF_3 \rightarrow CF + CF_4$ finally was discussed.

Introduction

The unimolecular dissociation of perfluoroethyl iodide

$$C_2F_5I \rightarrow C_2F_5 + I \quad \Delta H_0^\circ = 234.2 \text{ kJ mol}^{-1} \qquad (1)$$

is of interest for several reasons. On the one hand, like other perfluoroalkyl iodides, C_2F_5I may be of technical use replacing chlorine- and bromine-containing halons, the latter leading to ozone depletion (*e.g.*, ref. 1–4; ΔH_0° values in the present article are taken from ref. 5 and 6, except for C_2F_5I and C_2F_4I whose values are estimated by quantum-chemical calculations). On the other hand, it has interesting kinetic aspects. These are the issue of the present article.

There is, at first, the rate of the unimolecular dissociation of C_2F_5I. Next, like the thermal dissociation of $(C_2F_5)_3N$ leading to $3C_2F_5 + N$,[7] reaction (1) is a precursor for C_2F_5 which dissociates by the reaction

$$C_2F_5 \rightarrow CF_2 + CF_3 \quad \Delta H_0^\circ = 238.1 \text{ kJ mol}^{-1} \qquad (2)$$

Under typical shock tube conditions, the products CF_2 and CF_3 of reaction (2) decompose much more slowly than C_2F_5I and C_2F_5, see below. Instead of dissociating, they dimerize by the reactions

$$2CF_2 \rightarrow C_2F_4 \quad \Delta H_0^\circ = -279.1 \text{ kJ mol}^{-1} \qquad (3)$$

$$2CF_3 \rightarrow C_2F_6 \quad \Delta H_0^\circ = -389.4 \text{ kJ mol}^{-1} \qquad (4)$$

CF radicals could be formed in reactions like

$$CF_2 + CF_3 \rightarrow CF + CF_4 \quad \Delta H_0^\circ = -25.4 \text{ kJ mol}^{-1} \qquad (5)$$

which would lead to the stable product CF_4; CF might dimerize as well, forming the thermally stable C_2F_2 (or $C_2F + F$), see below. The rate constants of the various steps in the decomposition mechanism of C_2F_5I play a central role for the understanding of halon dissociation in general (see, *e.g.*, ref. 8). It, therefore, appears worthwhile to study C_2F_5I decomposition in detail.

While the unimolecular dissociations of CF_3I and C_3F_7I have been investigated extensively (see, *e.g.*, the shock wave and modelling studies of ref. 3, 9, and 10 for CF_3I and of ref. 4 for C_3F_7I), such work is lacking for C_2F_5I. There have been indirect isothermal, steady-state,[11,12] and CO_2-laser induced[11] pyrolysis experiments at moderate temperatures. To our knowledge,

[a] *INIFTA, Facultad de Ciencias Exactas, Universidad Nacional de La Plata, CONICET, Argentina. E-mail: juergen.troe@mpibpc.mpg.de*
[b] *Institut für Physikalische Chemie, Universität Göttingen, Tammannstr. 6, D-37077 Göttingen, Germany*
[c] *Max-Planck-Institut für biophysikalische Chemie, Am Fassberg 11, D-37077 Göttingen, Germany*

† Electronic supplementary information (ESI) available. See DOI: 10.1039/d0cp06414a

however, only a single high-temperature shock wave study has been performed for C_2F_5I.[13] This used the chemiluminescence process $I + I \rightarrow I_2 + h\nu$ to conclude on reaction (1). Because high reactant concentrations (0.2–1% of C_2F_5I in Ar) were employed, secondary reactions such as

$$C_2F_5 + C_2F_5I \rightarrow C_2F_6 + C_2F_4I \quad \Delta H_0^\circ = -24.5 \text{ kJ mol}^{-1} \quad (6)$$

or

$$1 + C_2F_5I \rightarrow C_2F_5 + I_2 \quad \Delta H_0^\circ = 85.4 \text{ kJ mol}^{-1} \quad (7)$$

(reaction (6) followed by the fast dissociation of C_2F_4I to $C_2F_4 + I$ and reaction (7) followed by the dissociation of I_2) were suggested to form the I atoms which then were used for detection. Other secondary reactions could not be identified, partly because the also recorded UV absorptions of the parent molecules and reaction products were found to be superimposed. As we have studied UV absorptions of possible reaction products separately before, we started a new approach to C_2F_5I dissociation in shock waves, analyzing superimposed absorption signals from reactants and products in the UV. In comparison to ref. 13, we were able to reduce the reactant concentrations in the shock waves down to 100 ppm in Ar, such that mechanistic aspects of the decomposition could be further investigated under simpler conditions.

The present work should also be seen in relation to dissociation studies of C_2F_5I using other excitation techniques. The UV photolysis of C_2F_5I, *e.g.*, has attracted attention as a fast, direct, dissociation process with high yields of excited $^2P_{1/2}$ iodine atoms (*e.g.*, ref. 14–17). The latter was considered useful for the construction of iodine photodissociation lasers (*e.g.*, ref. 18 and 19). The fast dissociation of C_2F_4I to $C_2F_4 + I$, which had been suggested to follow reaction (6),[13] has also been accessible.[20] UV laser flash photolysis and IR multiphoton excitation studies of C_2F_5I led to information[21,22] on the reverse of reaction (1) near room temperature, *i.e.* to the recombination

$$C_2F_5 + I \rightarrow C_2F_5I \quad \Delta H_0^\circ = -234.2 \text{ kJ mol}^{-1} \quad (8)$$

It was the aim of the present work to shed more light on the mechanism of C_2F_5I decomposition under high-temperature and low reactant concentration conditions. A theoretical modelling of the falloff curves for the unimolecular dissociation of C_2F_5I and its reverse reaction (8) was considered helpful for an analysis of the experimental results. As the present work uses UV absorption spectroscopy of the parent molecules and reaction products, quantitative knowledge of several high-temperature absorption coefficients was required. Such information was available from earlier publications referred to later. More information on absorption coefficients of C_2F_5I has been described recently.[23] As reaction (5) may lead to the formation of CF, the dimerization of this species, forming C_2F_2 (or leading to $C_2F + F$), was also modelled. Likewise, rate constants of other possible secondary reactions such as reactions (6) and (7) were inspected.

Experimental technique and results

Mixtures of 100 and 500 ppm of C_2F_5I in Ar were heated in shock waves. The mixtures (C_2F_5I from abcr with 99% purity and Ar from Air Liquide with 99.9999% purity) were prepared in vessels outside the shock tube before being introduced into the tube. The used tube (length of the test section 4.15 m and inner diameter 9.4 cm) has been described before (*e.g.* ref. 5, 10, and 23–34). The progress of the reaction was followed through windows placed into the wall of the tube, 5 cm in front of the reflecting end plate. Absorption measurements were made with a high pressure Xe arc lamp (Osram XBO 150 W/4), quartz monochromator (Zeiss M3), photomultiplier, and data acquisition arrangement. Absorption-time profiles were recorded behind incident and reflected waves. The available time for measurements behind the reflected shock was about 1.5 ms. As the observed spectra were all continuous or quasi-continuous, broad spectral widths of about ±1 nm could be used. Selected wavelengths from the range 200–280 nm were monitored. Temperatures for kinetic measurements were between 950 and 1500 K, bath gas concentrations [Ar] between 3×10^{-5} and 2×10^{-4} mol cm^{-3}.

The experiments led to a diversity of absorption-time profiles. Representative examples are shown in Fig. 1–5. The analysis of the signals used high-temperature absorption cross sections for C_2F_5I and C_2F_5 from ref. 23, for C_2F_4 from ref. 24, for CF_3I (formed by combination of CF_3 with I) from ref. 10 and 25, for CF_3 from ref. 23 and 26, for CF_2 from ref. 24 and 27, and for CF from ref. 28 (representative absorption cross sections at a typical temperature of 1200 K, for orientation, are given in Table 1). In addition, modelled rate constants such as summarized in Table 2 (for their determination, see the following sections and the ESI†) facilitated the analysis. Besides the dissociation reactions, their reverse recombination processes had also to be included. All dissociation and recombination reactions were in their falloff ranges such that suitable falloff expressions of the rate

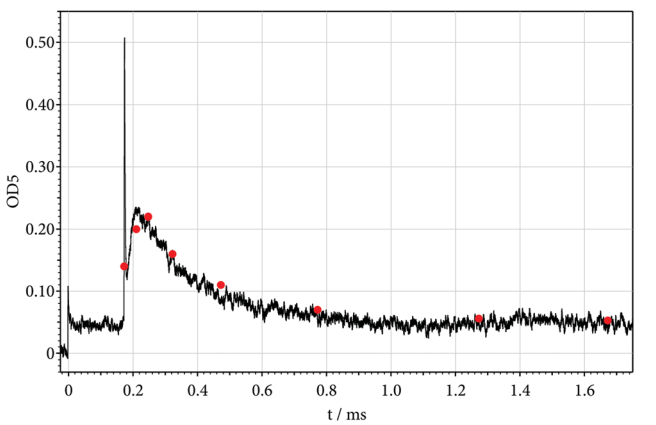

Fig. 1 Absorption-time profile recorded at 268.5 nm in the decomposition of C_2F_5I (reflected shock wave: T = 1195 K, 500 ppm of C_2F_5I in Ar, [Ar] = 1.3×10^{-4} mol cm^{-3}; OD5 = $\ln(I_0/I)$ with light intensity I and path length x = 9.4 cm, see text; ●: modelled points with data from Tables 1–3, k_5 fitted as $k_5 \approx 2 \times k_{-2,\infty}$ where $k_{-2,\infty} = k_{2,\infty}/K_{2,c}$, see text).

Table 1 Selected absorption cross sections σ near T = 1200 K, used for the analysis of Fig. 1–5, see text (* upper limits, estimated for 2000 K)

Species	Wavelength (nm)	σ (cm^2)	Ref.
C_2F_5I	280	4.1×10^{-19}	23
	268.5	3.3×10^{-19}	
C_2F_4	200	4.5×10^{-18}	24
CF_2	280	4.2×10^{-19}	27
	268.5	2.0×10^{-18}	
	248	6.8×10^{-18}	
	200	3.3×10^{-23}	
CF	248	1.0×10^{-17}	28*
	200	7.0×10^{-17}	

constants (with the parameters given in Table 2) had to be used. Without the mentioned spectroscopic and kinetic input parameters, an interpretation of the signals would have been considerably more difficult.

Fig. 1, first, shows a signal recorded at 268.5 nm, *i.e.* at the maximum of the room temperature spectrum of C_2F_5I.[14,35,36] The absorption steps at the arrival of the incident and reflected shocks (behind the two Schlieren peaks) allow one[23] to derive the absorption coefficients of C_2F_5I at 691 K (incident shock) and 1195 K (reflected shock; for a quantitative analysis, one has also to account for the absorption in front of the incident shock, using the known room temperature absorption coefficient). At the temperature of the reflected shock, obviously not only the disappearance of C_2F_5I but the appearance of a more strongly absorbing reaction product is observed which then disappears on a longer time scale. The identification of this absorber can be made using the rate constants characterized in Table 2. As k_1 (close to 10^5 s^{-1}) for Fig. 1 is markedly larger than k_2 (close to 2×10^4 s^{-1}), the decay of C_2F_5I is too fast to be resolved and the rising signal behind the reflected shock must be attributed to

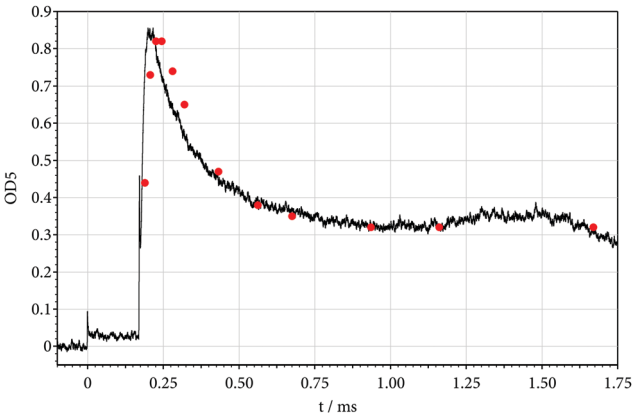

Fig. 2 As Fig. 1, but recorded at 248 nm (reflected shock wave: T = 1213 K, 530 ppm of C_2F_5I in Ar, [Ar] = 1.3×10^{-4} mol cm^{-3}; ●: modelled points with data from Tables 1–3, k_5 fitted as $k_5 \approx 1.5 \times k_{-2,\infty}$ where $k_{-2,\infty} = k_{2,\infty}/K_{2,c}$, see text).

CF_2 from reaction (2) (the maximum of CF_2 absorption of is located at 248 nm,[24,27] but the absorption of the broad quasi-continuum with increasing temperature increasingly extends to longer wavelengths, *i.e.* also to 268.5 nm).

Fig. 2 shows a signal recorded at 248 nm. Under the assumption that each decomposing C_2F_5I by reactions (1) and (2) leads to one CF_2, the initial rate of increase of the absorption behind the reflected shock in Fig. 2 allows one to derive an experimental value of k_2. The detailed analysis (accounting for the Schlieren signal) indeed leads to the modelled value following from Table 2, see below. Besides the initial increase of the signal due to the formation of CF_2, the decay of the signal behind the reflected shock must be explained. One finds that the decay of the CF_2 signal can mostly be attributed to the

Table 2 Modelled rate constants for dissociation reactions and their equilibrium constants (limiting high pressure dissociation rate constants k_∞ in s^{-1}, limiting low pressure dissociation rate constants k_0/[Ar] in cm^3 mol^{-1} s^{-1}, and weak collision center broadening factors $F_{cent} = F_{cent}^{sc} \times 0.64$ to be used in falloff expressions from ref. 39–41, equilibrium constants $K_c = k_{dis}/k_{rec}$ in mol cm^{-3}, *: experimental adjustment of $k_{1,\infty}$, $k_{1,0}$, and $K_{1,c}$ possible by adding a factor of exp(−600 K/T), see text)

Reaction	Modelled values	Ref.
(1) C_2F_5I (+Ar) → C_2F_5 + I (+Ar)	$k_{1,\infty} = 6.15 \times 10^{15}(T/1000\text{ K})^{-0.90}\exp(-28\,675\text{ K}/T)$, $k_{1,0} = [\text{Ar}]8.70 \times 10^{24}(T/1000\text{ K})^{-11.92}\exp(-33\,775\text{ K}/T)$, $F_{cent} = 0.059$(1000 K), 0.079(1500 K), $K_{1,c} = 6.15 \times 10^2(T/1000\text{ K})^{-1.36}\exp(-28\,675\text{ K}/T)$	Present*
(2) C_2F_5 (+Ar) → CF_2 + CF_3 (+Ar)	$k_{2,\infty} = 7.88 \times 10^{14}\exp(-27\,181\text{ K}/T)$, $k_{2,0} = [\text{Ar}]2.2810^{24}(T/1000\text{ K})^{-14.89}\exp(-35\,119\text{ K}/T)$, $F_{cent} = 0.054$(1000 K), 0.051(1500 K), $K_{2,c} = 5.75 \times 10^2(T/1000\text{ K})^{-0.24}\exp(-27\,181\text{ K}/T)$	ESI of 5
(3) C_2F_4 (+Ar) → 2CF_2 (+Ar)	$k_{3,\infty} = 6.0 \times 10^{15}(T/1000\text{ K})^{-0.87}\exp(-35\,050\text{ K}/T)$, $k_{3,0} = [\text{Ar}]1.07 \times 10^{23}(T/1000\text{ K})^{-9.7}\exp(-36\,660\text{ K}/T)$, $F_{cent} = 0.083$(1000 K), 0.079(1500 K), $K_{3,c} = 4.20 \times 10^4(T/1000\text{ K})^{-2.4}\exp(-35\,050\text{ K}/T)$	27 and 29
(4) C_2F_6 (+Ar) → 2CF_3 (+Ar)	$k_{4,\infty} = 1.2 \times 10^{18}(T/1000\text{ K})^{-0.52}\exp(-49\,316\text{ K}/T)$, $k_{4,0} = [\text{Ar}]2.61 \times 10^{27}(T/1000\text{ K})^{-13.8}\exp(-52\,289\text{ K}/T)$, $F_{cent} = 0.052$(1000 K), 0.041(1500 K), $K_{4,c} = 5.94 \times 10^4(T/1000\text{ K})^{-1.29}\exp(-49\,316\text{ K}/T)$	30
(17) C_2F_2 (+Ar) → 2CF (+Ar)	$k_{17,\infty} = 3.90 \times 10^{16}(T/1000\text{ K})^{-0.59}\exp(-58\,130\text{ K}/T)$, $k_{17,0} = [\text{Ar}]1.22 \times 10^{22}(T/1000\text{ K})^{-7.10}\exp(-59\,020\text{ K}/T)$, $F_{cent} = 0.19$(1000 K), 0.15(1500 K), $K_{17,c} = 3.60 \times 10^4(T/1000\text{ K})^{-2.15}\exp(-58\,230\text{ K}/T)$	Present
(18) CF_3I (+Ar) → CF_3 + I (+Ar)	$k_{18,\infty} = 5.94 \times 10^{15}(T/1000\text{ K})^{-2.20}\exp(-28\,928\text{ K}/T)$, $k_{18,0} = [\text{Ar}]5.44 \times 10^{21}(T/1000\text{ K})^{-10.46}\exp(-31\,358\text{ K}/T)$, $F_{cent} = 0.14$(1000 K), 0.13(1500 K), $K_{18,c} = 8.80 \times 10^2\ (T/1000\text{ K})^{-2.72}\exp(-28\,928\text{ K}/T)$	10

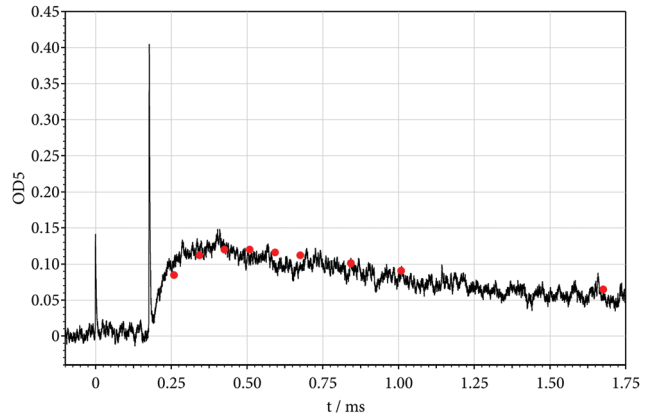

Fig. 3 As Fig. 1, but recorded at 248 nm (reflected shock wave: T = 1117 K, 108 ppm of C_2F_5I in Ar, and [Ar] = 1.4 × 10^{-4} mol cm^{-3}; ●: modelled points with data from Tables 1–3, k_3 increased by a factor of 2 and k_5 fitted as $k_5 \approx 10 \times k_{-2,\infty}$ where $k_{-2,\infty} = k_{2,\infty}/K_{2,c}$, see text).

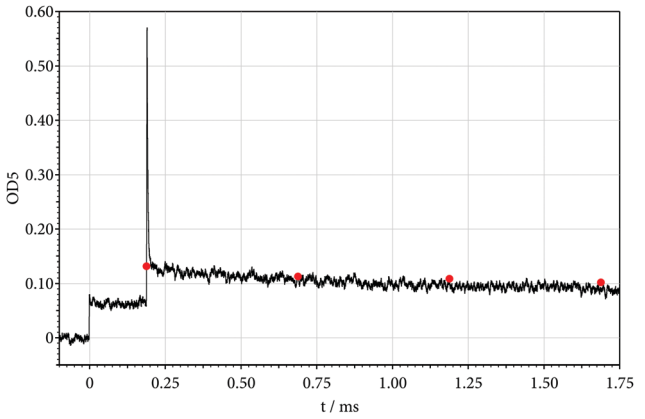

Fig. 5 As Fig. 1, but recorded at 280 nm (reflected shock wave: T = 970 K, 497 ppm of C_2F_5I in Ar, [Ar] = 1.6 × 10^{-4} mol cm^{-3}; ●: modelled points with data from Tables 1–3, k_1 and $K_{1,c}$ decreased by a factor of exp(−600 K/T), see text).

known dimerization of CF_2 (with rate constants following from Table 2). One, furthermore, observes that the maximum of the signal is markedly smaller than expected for a simple mechanism of reactions (1) and (2) alone. This is attributed to a contribution from reaction (5) which converts CF_2 into less reactive species, see below.

A dependence of the CF_2 signal on the reactant concentration is documented in Fig. 3 where the initial C_2F_5I concentration has been decreased by about a factor of 5 in comparison to Fig. 1 and 2. The initial rate of CF_2 formation again is well explained by that of C_2F_5 dissociation ($k_2 \approx 2 \times 10^4$ s^{-1}). The decay of the CF_2 signal on the other hand is markedly slower than that of Fig. 1 and 2, indicating a more complicated kinetics of CF_2 disappearance than explained by dimerization alone, see below.

While a contribution from the parent C_2F_5I to the signal behind the reflected shock at 248 nm is only of minor importance and can be accounted for, one may also look for absorptions from other species. For this reason, we inspected signals at shorter wavelengths. Fig. 4 shows an example recorded at 200 nm. At this wavelength, a contribution of CF_2 to the signal can safely be neglected.[24] Instead, the absorption from stronger absorbers, forming during the reaction here dominates. One of these can be identified as C_2F_4.[24] First, the rise time of the signal corresponds to the dimerization of CF_2 by reaction (3).[27,29] Second, at higher temperatures where C_2F_4 thermally decomposes, the final signals are consistent with the temperature dependence of the $C_2F_4 \leftrightarrows 2CF_2$ equilibrium.[27] Third, the absolute values and the wavelength dependence of the signals agree with the known results for C_2F_4.[24] A second contribution to the signal may arise from the even stronger absorber CF formed by reactions like reaction (5).[28] Unfortunately the present work could not provide more insight into the kinetics of CF radicals. It was, therefore, also not clear whether "irregularities" of the signals at late time in Fig. 2 and 4 (after about 1 ms) were due to such reactions, or simply marked the end of the observation time in the shock wave experiments.

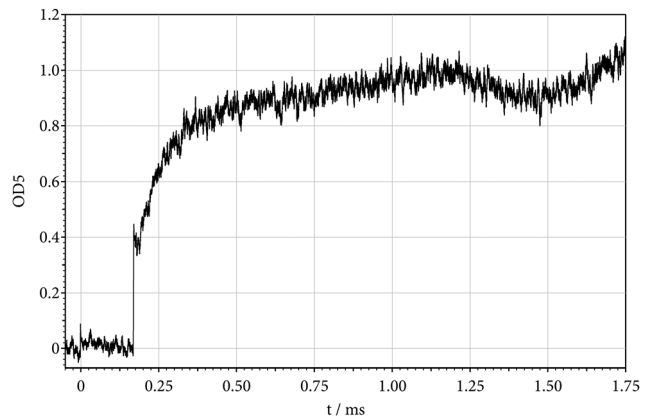

Fig. 4 As Fig. 1, but recorded at 200 nm (reflected shock wave at t = 0.18 ms: T = 1255 K, 533 ppm of C_2F_5I in Ar, and [Ar] = 1.2 × 10^{-4} mol cm^{-3}).

In order to record signals with contributions mostly from C_2F_5I, we finally inspected absorption-time profiles at 280 nm, *i.e.* on the long-wavelength tails of the C_2F_5I and CF_2 absorption continua. Fig. 5 shows a signal recorded for a temperature lower than those used in Fig. 1–4. Here, CF_2 formation is too slow to disturb the absorption signal from C_2F_5I to a major extent, but the decay of C_2F_5I becomes visible.

The overall mechanism of C_2F_5I dissociation, even at reactant concentrations as low as 100 ppm in Ar, apparently was not only determined by the primary first-order dissociation of C_2F_5I, but by several secondary first- and second- order reaction steps and their reverse reactions (equilibrium constants are included in Table 2). A modelling of the corresponding rate constants appeared helpful for a start of the analysis of signals like Fig. 1–5. This modelling is described in the following section (as well as in the ESI†).

Modelling of rate constants for the unimolecular dissociation of C_2F_5I

Our quantum-chemical characterization of the potential energy surface for C_2F_5I dissociation (1) closely followed the procedure

outlined for CF_3I dissociation in ref. 10 (and its ESI) and needs not to be repeated here. The derived electronic potential for the C_2F_5–I bond is illustrated in Fig. S1 of the present ESI.† The potential can be approximated by a Morse potential with a Morse parameter $\beta = 1.51$ Å^{-1} (for C_2F_5–I distances larger than 2.2 Å) or $\beta = 1.76$ Å^{-1} (for C_2F_5–I distances larger than 3.25 Å). The quanta of the bending modes of C_2F_5I, which disappear during bond-breaking, decrease exponentially with increasing C_2F_5–I bond length (with decay parameters $\alpha = 0.53(\pm0.01)$ Å^{-1}, see Fig. S2 of the ESI†). The decrease of the rotational constant $(B + C)/2$ of the decomposing C_2F_5I is also fitted such as illustrated in Fig. S3 of the ESI.† The latter is required for the determination of the centrifugal barriers which can be represented by $E_0(J) \approx E_0(J = 0) + C_\nu[J(J + 1)]^\nu$ with $C_\nu = hc\cdot1.14 \times 10^{-3}$ cm^{-1} and $\nu = 1.17$. Neglecting the anisotropy of the potential, *i.e.* using phase space theory (PST), high pressure recombination rate constants for reaction (8) of $k^{PST}_{rec,\infty} = (4–6) \times 10^{13}$ cm^3 mol^{-1} s^{-1} are obtained between 750 and 2000 K (see the modelling results in Table 2). The anisotropy of the potential introduces "rigidity" and reduces $k_{rec,\infty}$ to values below $k^{PST}_{rec,\infty}$. The classical trajectory version of the statistical adiabatic channel model (SACM/CT) of ref. 37 provides a simple approach to express this reduction as a function of the ratio α/β, here shown to be about 0.3 (one notes that this ratio in the present case is somewhat below the "standard value" 0.5,[38] *i.e.* it corresponds to a comparably rigid potential). Table 3 shows the results for $k_{rec,\infty}$ which can be approximated by

$$k_{rec,\infty} \approx 1.0 \times 10^{13} (T/1000\ \text{K})^{0.46}\ \text{cm}^3\ \text{mol}^{-1}\ \text{s}^{-1} \quad (9)$$

The corresponding dissociation rate constants $k_{dis,\infty}$ in Table 2 are represented by

$$k_{dis,\infty} \approx 6.15 \times 10^{15}(T/1000\ \text{K})^{-0.90} \exp(-28\,675\ \text{K}/T)\ \text{s}^{-1} \quad (10)$$

It appears worthwhile to compare the modelled high-pressure recombination rate constants for 300 K, *i.e.* $k_{rec,\infty}(300\ \text{K}) \approx 5.5(\pm3) \times 10^{12}$ cm^3 mol^{-1} s^{-1}, with the measurements from ref. 21 and 22 which led to a value of $1.2(\pm0.4) \times 10^{13}$ cm^3 mol^{-1} s^{-1}. Within the estimated uncertainties of either approach, the results appear sufficiently close.

The calculation of the limiting low-pressure rate constant $k_{dis,0}$ followed the procedure described in ref. 39 with the required parameters C_ν, ν, and $E_0(J)$ for the centrifugal barriers as given above (for other parameters, see the ESI†). Collision efficiencies and the corresponding average (total) energies transferred per collision $\langle\Delta E\rangle$ as usual had to be estimated.

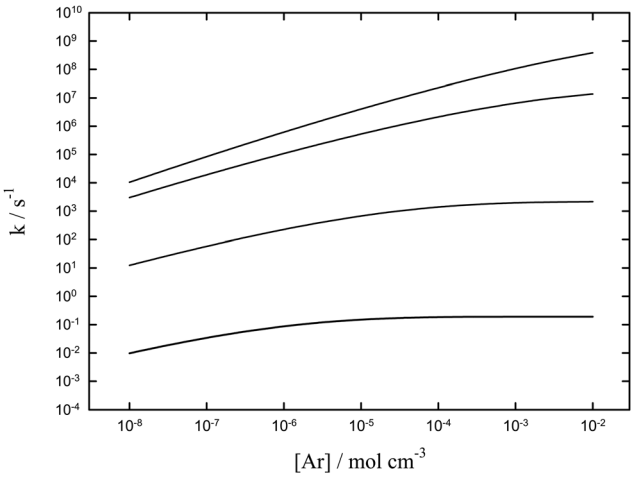

Fig. 6 Modelled falloff curves for the unimolecular dissociation of C_2F_5I in Ar (calculations for 750, 1000, 1500, and 2000 K from bottom to top; see text and ESI†).

Like in previous work, we used a value of $\langle\Delta E\rangle/hc \approx -100$ cm^{-1} for a start. This led to

$$k_{dis,0} \approx [\text{Ar}]8.7 \times 10^{24}(T/1000\ \text{K})^{-11.92} \exp(-33\,775\ \text{K}/T)\ \text{cm}^3\ \text{mol}^{-1}\ \text{s}^{-1} \quad (11)$$

Falloff expressions for the transition of k_1 from $k_{dis,0}$ to $k_{dis,\infty}$ were expressed in the form proposed in ref. 39–42. The required weak collision "center broadening factors" $F_{cent} = F^{sc}_{cent} \times 0.64$ were estimated with the method of ref. 39–41. Values of $F_{cent} \approx 0.063$, 0.059, 0.079, and 0.12 were derived for T/K = 750, 1000, 1500, and 2000, respectively. The finally obtained falloff curves are shown in Fig. 6. The figure well documents the shift of the falloff curves with temperature. At a bath gas concentration [Ar] = 10^{-4} mol cm^{-3} and $T \leq 750$ K, the reaction is close to the high-pressure limit, while it is closer to the low-pressure limit at $T \geq 1500$ K. Intermediate falloff effects thus are important for all conditions of the present work. Modelled dissociation and recombination rate constants are summarized in Table 3. Values for $k_{rec,\infty}$ are compared with $k^{PST}_{rec,\infty}$, illustrating the effects of the anisotropy of the potential. Furthermore, the positions of the "centers of the falloff curves" $[\text{Ar}]_{cent}$ are given, *i.e.* the values of [Ar] for which $k_{dis,0} \approx k_{dis,\infty}$. The increase of $[\text{Ar}]_{cent}$ with increasing T quantifies the shift of the falloff curves with temperature. It also appears important to estimate the uncertainty of $k_{dis,\infty}$ caused by the uncertainty of the reaction enthalpy. The modelling of the signal of Fig. 5 and of the rate constants $k_1(T)$ described below

Table 3 Modelled rate constants for dissociation and recombination of C_2F_5I, $k_{dis} = k_1$ and $k_{rec} = k_8$ ($k^{PST}_{rec,\infty} = k_{rec}$ from Phase Space Theory (PST); $k^{PST}_{rec,\infty}$ and $k_{rec,\infty}$ in cm^3 mol^{-1} s^{-1}; $k_{dis,\infty}$ in s^{-1}; $k_{dis,0}$/[Ar] in cm^3 mol^{-1} s^{-1}; F_{cent}: weak collision center broadening factors; $[\text{Ar}]_{cent}$ in mol cm^{-3}: centers of the falloff curves, see text)

T/K	$k^{PST}_{rec,\infty}$	$k_{rec,\infty}$	$k_{dis,\infty}$	$k_{dis,0}$/[Ar]	F_{cent}	$[\text{Ar}]_{cent}$
750	4.40×10^{13}	8.89×10^{12}	1.99×10^{-1}	4.20×10^{7}	0.063	4.7×10^{-9}
1000	4.76×10^{13}	1.00×10^{13}	2.16×10^{3}	1.86×10^{10}	0.059	1.2×10^{-7}
1500	5.46×10^{13}	1.22×10^{13}	2.14×10^{7}	1.02×10^{12}	0.079	2.1×10^{-5}
2000	6.01×10^{13}	1.39×10^{13}	1.95×10^{9}	1.62×10^{12}	0.12	1.2×10^{-3}

suggests an increase of ΔH_0° by about 5 kJ mol^{-1} which adds a factor of about exp(−600 K/T) to eqn (10) and (11) as well as $K_{1,c}$ in Table 2. Finally, it appears of interest to compare the present modelling results for k_1 with values obtained from the iodine chemiluminescence experiments of ref. 13. The values for k_1 from the latter work at 1100 K are about a factor of two larger than the present modelling whereas they nearly agree near 1300 K.

Modelling of rate constants for secondary reactions

In this section we describe modelling results for reactions which may play a role as secondary processes in the decomposition mechanism of C_2F_5I. As the falloff curves for the dissociation reactions of C_2F_4, C_2F_5, C_2F_6, and CF_3I and their reverse recombination (or dimerization) reactions had been characterized before, they need not to be described here again (see their parameters in Table 2). We only performed a further modelling of C_2F_2 dissociation and the reverse CF dimerization rates. These data are needed in case that CF is formed by some secondary reactions (details of this modelling are described in the ESI† and the results are included in Table 2). CF is a particularly strong absorber over the wavelength range 200–280 nm studied in the present work, such that eventual contributions from CF to the recorded signals had to be carefully considered. CF, *e.g.*, could be formed by reaction (5); high-energy dissociation channels of C_2F_4, C_2F_5, and C_2F_6, however, could also play some role. For this reason, we determined minimum-energy path (MEP) potentials of the corresponding processes using the quantum-chemical techniques mentioned above. Fig. 7 shows the results for reaction (5) and the dissociation of C_2F_5. The calculations first show that the MEP pathway from CF_2 + CF_3 through bound C_2F_5 to CF + CF_4 involves a high energy barrier (TS) of 224.6 kJ mol^{-1}. This would rule out reaction (5) as a pathway for CF formation.

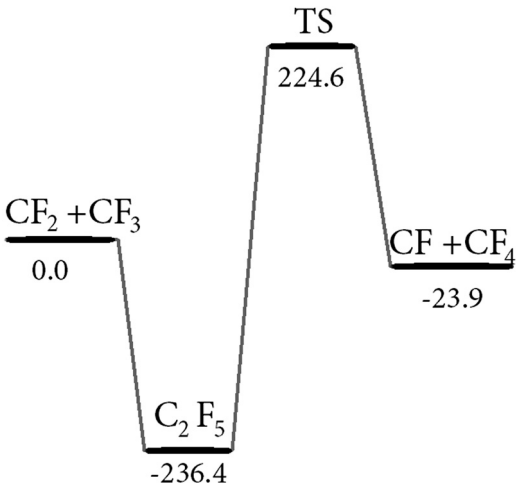

Fig. 7 Schematic energy diagram for reactions (2) and (5) (energies in kJ mol^{-1}; from *ab initio* composite G4 model and Intrinsic Reaction Coordinate (IRC) calculations; see text and ESI†).

However, one may imagine that the exothermic reaction proceeds as a roaming radical process (analogous to processes described in ref. 43–45), skirting "outside" along the barrier of the TS and avoiding the passage of the C_2F_5 intermediate. While this looks like an attractive possibility, its confirmation by trajectory calculations on a full potential for C_2F_5 is not within the scope of the present article.

A high-energy pathway of C_2F_4 dissociation forming CF under the present conditions apparently is too endothermic ($\Delta H_0^\circ = 160.5$ kJ mol^{-1}, see the MEP potential of Fig. S13 of the ESI†). On the other hand, the exothermic pathway $CF_3 + CF_3 \rightarrow CF_2 + CF_4 (\Delta H_0^\circ = -181.2$ kJ mol$^{-1})$, followed by reaction (5) *i.e.* by $CF_2 + CF_3 \rightarrow CF + CF_4 (\Delta H_0^\circ = -25.4$ kJ mol$^{-1})$, could also lead to CF (see the MEP potential for CF_3 + CF_3 in the ESI,† Fig. S14). The formation of some CF in the decomposition mechanism thus also appears possible. It should finally be mentioned that absorption-time profiles like Fig. 4 were also observed in the study of the decomposition of CF_3I (see Fig. 6 of ref. 10); these signals were tentatively attributed to the formation of IF. However, an interpretation analogous to that from the present work presents a more attractive alternative. If CF is formed, besides the dimerization 2CF → C_2F_2 a reaction 2CF → C_2F + F should also be considered (see details in ESI†-III).

Besides pathways for CF formation and rates for CF dimerization, we also modelled the bimolecular reactions (6) and (7) between the parent C_2F_5I and its dissociation products C_2F_5 and I. These reactions could be important for higher reactant concentrations and they were used for the observation of the C_2F_5I decomposition reaction by detection of I_2 in ref. 13, see above. Reaction (6) could proceed on the two exothermic pathways

$$C_2F_5 + C_2F_5I \rightarrow C_2F_6 + CF_3CFI \quad (\Delta H_0^\circ = -46.1 \text{ kJ mol}^{-1}) \tag{12}$$

$$C_2F_5 + C_2F_5I \rightarrow C_2F_6 + CF_2CF_2I \quad (\Delta H_0^\circ = 0.84 \text{ kJ mol}^{-1}) \tag{13}$$

but in both cases high energy barriers TS are involved. The calculations described in the ESI† led to activation enthalpies of 164.8 kJ mol^{-1} for reaction (12) and 181.1 kJ mol^{-1} for reaction (13). TST calculations of the rate constants were represented by

$$k_{12} \approx 2.7 \times 10^{10} (T/1000 \text{ K})^{3.1} \exp(-1985 \text{ K}/T) \text{ cm}^3 \text{ mol}^{-1} \text{ s}^{-1} \tag{14}$$

$$k_{13} \approx 1.2 \times 10^{11} (T/1000 \text{ K})^{3.1} \exp(-21850 \text{ K}/T) \text{ cm}^3 \text{ mol}^{-1} \text{ s}^{-1} \tag{15}$$

corresponding to $k_{12} = 6.5 \times 10^1$ cm^3 mol^{-1} s^{-1} and $k_{13} = 4.0 \times 10^1$ cm^3 mol^{-1} s^{-1} at $T = 1000$ K. In contrast to these reactions, for reaction (7) between I and C_2F_5I no activation barrier was found beyond the endothermicity. This is consistent with the experiments of ref. 11, 12, and 46 which determined an activation energy close to zero for the reverse reaction

$I_2 + C_2F_5 \rightarrow I + C_2F_5I$. Converting the experimental results for this reaction with the equilibrium constants led to

$$k_7 \approx 3.6 \times 10^{13} \exp(-7460\ \mathrm{K}/T)\ \mathrm{cm^3\ mol^{-1}\ s^{-1}} \quad (16)$$

corresponding to $k_7 \approx 2 \times 10^{10}$ cm^3 mol^{-1} s^{-1} at T = 1000 K. Clearly reaction (6) thus can be neglected, while reaction (7) must be accounted for in experiments using larger concentrations than those of the present work.

Analysis of experimental absorption profiles

As emphasized before, the analysis of experimental absorption-time profiles is greatly facilitated by the modelling results described in the two previous sections. In the following this will be demonstrated for the shown examples of experimental signals. As the considered dissociation and the reverse recombination reactions are all in their falloff ranges, the falloff expressions from ref. 39–41 for the [Ar]-dependence of the rate constants were used. The required falloff parameters and equilibrium constants $K_{i,c}$ were taken from Tables 2 and 3.

For the lowest temperatures of the present study (and the given [Ar]), k_1 exceeds k_2 (*e.g.*, $k_1 = 6.7 \times 10^2$ s^{-1} *vs.* $k_2 = 2.0 \times 10^2$ s^{-1} for Fig. 5). The signal of Fig. 5 at 280 nm, therefore, is dominated by the faster decay of C_2F_5I and not by the much slower formation of CF_2. Fig. 5 includes a modelled absorption-time profile, accounting for the contributions from C_2F_5I and CF_2. In spite of the superposition of the two absorptions, signals like Fig. 5 can be used to derive experimental values of k_1 independent of the precise value of k_2. One should note, however, that in later stages of the reaction one must account for the onset of the recombination reaction (8), *i.e.* of $C_2F_5 + I \rightarrow C_2F_5I$. This can be done with the help of the equilibrium constant $K_{1,c}$ given in Table 2. Within the relatively large experimental uncertainty (because of the superposition of the two absorptions estimated to be about a factor of two), the derived values of k_1 agree with the [Ar]-dependent modelling results such as illustrated by the Arrhenius plot of Fig. 8. An improved fit was obtained (both in Fig. 5 and 8) if ΔH_0° was increased from the value calculated in the present work (see the ESI†) by about 5 kJ mol^{-1}. One should mention one further complication: according to the equilibrium constants from Table 2, one would have expected a dissociation of only a few percent of C_2F_5I until equilibrium in Fig. 5 is reached whereas the signal decays to smaller values. This observation, however, is explained by the onset of reactions (2) and (5), and possibly some contribution from reaction (6).

Observations at 268.5 nm, such as illustrated in Fig. 1, like in Fig. 5 are characterized by the superposition of absorptions from C_2F_5I and CF_2. As the absorption cross sections of both species are known (see Table 1), the signals nevertheless can be simulated. With the modelled values for k_1 and k_2 (as well as the other rate constants from Table 1, in particular k_3), results such as included in Fig. 1 are obtained, validating the given interpretation of the signals.

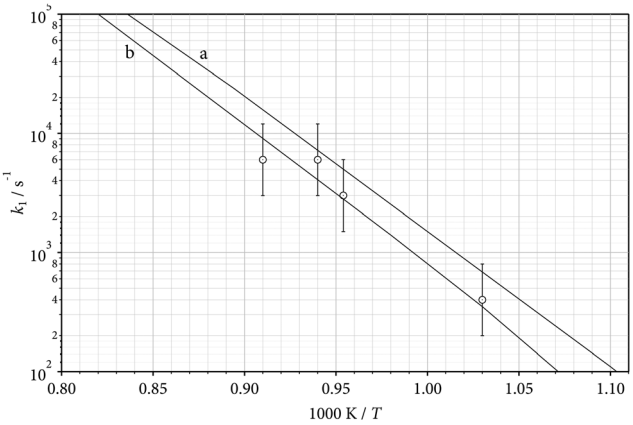

Fig. 8 Pseudo-first order rate constants k_1 of the unimolecular dissociation of C_2F_5I at [Ar] = 1.4 × 10^{-4} mol cm^{-3} (full line: modelling results from Tables 1–3, curve a for $\Delta H_0^\circ = 234$ kJ mol^{-1}, curve b for $\Delta H_0^\circ = 239$ kJ mol^{-1}; symbols: examples of experimental results from the present work with estimated error bars, see text).

At 248 nm the absorption cross section of CF_2 by far exceeds that of C_2F_5I. As C_2F_5I decomposes much more rapidly than CF_2, the formation and consumption of the latter species can well be studied without interference from C_2F_5I. Assuming that one C_2F_5 is produced per one dissociating C_2F_5I, the initial rise of the CF_2 signal can be attributed to CF_2 formation by reaction (2) alone. The modelling of the complete mechanism also allows one to predict the maximum of the signal. With reactions (1)–(4) one predicts a larger signal than observed. This can be attributed to reaction (5) which efficiently converts CF_2 and CF_3 into the less active species CF and CF_4. The reduction of the maximum of the signals allows one to fit k_5. One obtains values of the order of the limiting high pressure rate constant for the recombination of CF_2 and CF_3 forming C_2F_5 (*e.g.*, for Fig. 2, $k_5 \approx 2 \times k_{-2,\infty}$ where $k_{-2,\infty} = k_{2,\infty}/K_{2,c}$; unfortunately the fit of k_5 is markedly influenced by uncertainties in k_1, k_2, k_3, and k_4, such that more precise determinations have to wait for studies in simpler reaction systems; so far the uncertainty of k_5 is estimated to be about a factor of 4).

The contribution of reaction (5) weakens when the reactant concentration is further decreased. Fig. 3 shows an example with a reactant concentration as low as about 100 ppm. The mechanism here indeed is dominated by reactions (1)–(4). Measurements at 248 nm were also performed behind incident shock waves, such that [Ar] could be varied between 2 × 10^{-5} and 2 × 10^{-4} mol cm^{-3}. The comparison between experimental and modelled rate constants in the falloff range of reaction (2) is illustrated in Fig. 9 for low and high [Ar]. An agreement with the modelled rate constants within about a factor of 2 was obtained, similar to that of Fig. 8.

While the signals of Fig. 1, 3 and 5 could well be modelled with the data from Tables 1–3 and fitted values of k_5, the modelling of Fig. 4 met with difficulties. Although the time dependence of the increasing signal at 200 nm corresponds well to the formation of C_2F_4 by the dimerization reaction (3), the signal is larger than explained by C_2F_4 formation alone. Obviously, there is an important, additional, contribution to

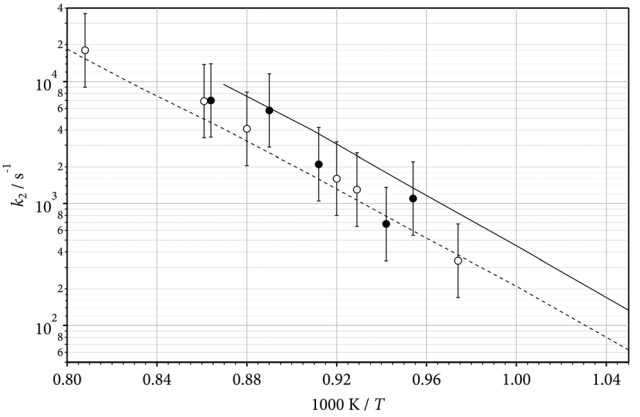

Fig. 9 Pseudo-first order rate constants k_2 of the unimolecular dissociation of C_2F_5 (2) (full line: modelling results for [Ar] = 1.5×10^{-4} mol cm^{-3}, dashed line: modelling results for [Ar] = 2.8×10^{-5} mol cm^{-3}, see Table 2 and ref. 7; symbols: experimental results from the present work with estimated error bars, see text; open circles for [Ar] = 2.8×10^{-5} mol cm^{-3}, filled circles for [Ar] = 1.5×10^{-4} mol cm^{-3}).

the signal from the strong absorber CF formed by reaction (5). As only upper limits of the absorption cross section of CF at 200 nm are available (for temperatures near 2000 K) and more precise values of k_5 are needed, a modelling of the signal of Fig. 4 does not yet appear warranted. This also concerns the ''irregularities'' of the signal after about 1 ms (mentioned for Fig. 2 above; one should also mention that the step of the signal at the arrival of the reflected shock wave is due to C_2F_5I from an absorption band located at wavelengths below 200 nm[2,3]). Because of these complications, the present reaction system did not appear suitable for further studies of CF reactions.

Conclusions

The described UV absorption study has provided insight into the dissociation mechanism of C_2F_5I. It has allowed us to analyze the absorption-time profiles of the dissociating C_2F_5I and of reaction products like CF, CF_2 and C_2F_4. As the absorptions of these species are all superimposed, modelled rate constants and separately determined absorption cross sections facilitated the analysis of the recorded signals. The diversity of the signals allowed for a validation of the modelled rate constants and the decomposition mechanism. The detection of iodine atoms by ARAS (atomic resonance absorption spectroscopy) like in ref. 3 and 4 (studying the dissociations of CF_3I and C_3F_7I), would have allowed to work with even lower reactant concentrations than the present UV absorption technique and provided a more direct access to the unimolecular dissociation of C_2F_5I. However, monitoring UV absorption signals of other species at higher reactant concentrations has provided insight into the decomposition mechanism and its secondary reactions.

A number of points deserve particular mention: (i) even under the low concentration conditions of the present work, the reverse of all dissociation reactions had to be included; (ii) falloff effects of all dissociation and recombination reactions had to be accounted for; (iii) the dominant absorption contributions came from C_2F_5I, CF_2, C_2F_4, and CF, however, with relative importance varying with wavelength and temperature; (iv) CF probably was formed by a roaming radical process $CF_2 + CF_3 \rightarrow CF + CF_4$ (5) bypassing the bound C_2F_5 intermediate (with a rate constant of the order of, but somewhat larger than, the limiting high pressure rate constant for the recombination of CF_2 and CF_3 forming C_2F_5); (v) CF apparently dimerizes to C_2F_2. (vi) besides I atoms, the most stable end products of the decomposition under the conditions of the described work probably are CF_4 and C_2F_2.

The present study illustrates again the benefit of combining kinetic measurements with rate constant modellings. Experimentally determined rate constants for the dissociations of C_2F_5I and C_2F_5 were shown to agree well with modelled values which then validates the use of the modelled rate constants for extrapolation into unexplored ranges.

Conflicts of interest

There are no conflicts to declare.

Acknowledgements

Financial support of this work by the Deutsche Forschungsgemeinschaft (Project TR 69/21-3) is gratefully acknowledged. Open Access funding provided by the Max Planck Society.

References

1 S. Solomon, J. B. Burkholder, A. R. Ravishankara and R. R. Garcia, Ozone Depletion and Global Warming Potentials of CF_3I, *J. Geophys. Res.*, 1994, **99**, 20.929–20.935.
2 Yu. N. Shebeko, V. V. Azatyan, I. A. Bolodian, V. Y. Navzenya, S. N. Koyplov, D. Y. Shebeko and E. D. Zamishevski, The Influence of Fluorinated Hydrocarbons on the Combustion of Gaseous Mixtures in a Closed Vessel, *Combust. Flame*, 2000, **121**, 542–547.
3 N. S. Bystrov, A. V. Emelianov, A. V. Eremin and P. I. Yatsenko, Direct Measurements of Rate Coefficients for Thermal Decomposition of CF_3I using Shock-Tube ARAS technique, *J. Phys. D: Appl. Phys.*, 2018, **51**, 1–8.
4 N. S. Bystrov, A. V. Emelianov, A. V. Eremin, B. Loukhovitski, A. Sharipov and P. I. Yatsenko, Direct Measurements of C_3F_7I Dissociation Rate Constant using a Shock-Tube ARAS technique, *Int. J. Chem. Kinet.*, 2019, **51**, 206–214.
5 E. Goos, A. Burcat and B. Ruscic, *Extended Third Millenium Ideal Gas and Condensed Phase Thermochemical Database for Combustion with Updates from Active Thermochemical Tables*. http://burcat.technion.ac.il/div September 2005, January 2015.
6 J. B. Burkholder, J. P. D. Abbatt, R. E. Huie, M. J. Kurylo, D. M. Wilmouth, S. P. Sander, J. R. Barker, C. E. Kolb, V. L. Orkin and P. H. Wine, Chemical Kinetics and Photochemical Data for Use in Atmospheric Studies Evaluation

Number 18, JPL Publication 15 – 10 2015, Jet Propulsion Laboratory, Pasadena.

7 C. J. Cobos, K. Hintzer, L. Sölter, E. Tellbach, A. Thaler and J. Troe, Shock Wave and Modelling Study of the Dissociation Pathways of $(C_2F_5)_3N$, *Phys. Chem. Chem. Phys.*, 2019, **21**, 9785–9792.

8 K. Li, E. M. Kennedy and B. Z. Dlugogorski, Experimental and Computational Studies of the Pyrolysis of $CBrF_3$, and the Reaction of $CBrF_3$ with CH_4, *Chem. Eng. Sci.*, 2000, **55**, 4067–4078.

9 S. S. Kumaran, M.-C. Su, K. P. Lim and J. V. Michael, Thermal Decomposition of CF_3I using I-atom Absorption, *Chem. Phys. Lett.*, 1995, **243**, 59–63.

10 C. J. Cobos, L. Sölter, E. Tellbach and J. Troe, Falloff Curves and Mechanism of Thermal Decomposition of CF_3I in Shock Waves, *Phys. Chem. Chem. Phys.*, 2019, **21**, 23892–23899.

11 S. L. Dobychin, V. I. Mashendzhinov, V. I. Mishin, V. N. Semenov and V. S. Shpak, Kinetics of Thermal Decomposition of Perfluoroalkyl Iodides and D(R-I) Binding Energy, R = CF_3, C_2F_5, n-C_3F_7, iso-C_3F_7, *n*-C_4F_9, *tert*-C_4F_9, *Dokl. Akad. Nauk SSSR*, 1990, **312**, 1166–1168.

12 G. A. Skorobogatov, B. P. Dymov and V. K. Khripun, Determination of Rate Constants and Equilibrium Constants of RI ↔ R + I and I + RI ↔ I_2 + R for R = CF_3, C_2F_5, or C_4F_9, *Kinet. Katal.*, 1991, **32**, 252–259.

13 I. S. Zaslonko, Yu. K. Mukoseev, G. A. Skorobogatov, V. N. Smirnov and V. K. Khripun, Rate Constant of Thermal Dissociation of Gaseous C_2F_5I, *Kinet. Katal.*, 1991, **32**, 468–473.

14 W. H. Pence, S. L. Baughcum and S. R. Leone, Laser UV Photofragmentation of Halogenated Molecules. Selective Bond Dissociation and Wavelength-Specific Quantum Yields for Excited $I(^2P_{1/2})$ and $Br(^2P_{1/2})$ Atoms, *J. Phys. Chem.*, 1981, **85**, 3844–3851.

15 D. Krajnovich, L. J. Butler and Y. T. Lee, UV Photodissociation of C_2F_5Br, C_2F_5I, and 1,2-C_2F_4BrI, *J. Phys. Chem.*, 1984, **81**, 3031–3047.

16 A. V. Baklanov, M. Aldener, B. Lindgren and U. Sassenberg, R2PI Detection of the Quantum Yields of $I(^2P_{1/2})$ and $I(^2P_{3/2})$ in the Photodissociation of C_2F_5I, *n*-C_3F_7I, *i*-C_3F_7I and CH_3I, *Chem. Phys. Lett.*, 2000, **325**, 399–404.

17 A. V. Baklanov, G. A. Bogdanchikov, M. Aldener, U. Sassenberg and A. Persson, Nanosecond and Femtosecond Probing of the Dynamics of the UV-photodissociation of Perfluoroethyliodide C_2F_5I, *J. Chem. Phys.*, 2001, **115**, 11157–11165.

18 K. Hohla and K. L. Kompa, in *Handbook of Chemical Lasers*, ed. R. W. F. Gross and J. F. Bott, Wiley, New York, 1976.

19 G. A. Skorobogatov, Chemical Processes in Active Volume of Photodissociative Iodine Laser, *Czech. J. Phys.*, 1991, **41**, 1189–1203.

20 D. Zhong and A. H. Zewail, Femtosecond Real-Time Probing of Reactions. 23. Studies of Temporal, Velocity, Angular, and State Dynamics from Transition States to Final Products by Femtosecond-Resolved Mass Spectrometry, *J. Phys. Chem. A*, 1998, **102**, 4031–4058.

21 A. M. Velichko, E. B. Gordon, A. A. Nadeikin, A. I. Nikitin and V. L. Tal'roze, Multiphoton Dissociation and Fragmentation of C_2F_5I, *High Energ. Chem.*, 1986, **20**, 468–471.

22 G. A. Skorobogatov, V. G. Seleznev and O. N. Slesar, Method of Overlapping Relaxations Measurement of the Absolute Rate Constants of Competing Reactions of a C_nF_{2n+1} Radical and $I(^2P_{1/2})$, $I(^2P_{3/2})$ Atoms in the Gas Phase, *Dokl. Phys. Chem.*, 1976, **231**, 1292–1295.

23 C. J. Cobos, K. Hintzer, L. Sölter, E. Tellbach, A. Thaler and J. Troe, Shock Wave and Modelling Study of the UV Spectra of Perfluorocarbon Iodide and Perfluorocarbon Radicals, *Combust. Flame*, 2021, **224**, 177–182.

24 C. J. Cobos, G. Knight, L. Sölter, E. Tellbach and J. Troe, Kinetic and Spectroscopic Studies of the Reaction of CF_2 with H_2 in Shock Waves, *J. Phys. Chem. A*, 2017, **121**, 7827–7834.

25 L. Brouwer and J. Troe, Shock Wave Study of the UV Spectrum of CF_3I, *Chem. Phys. Lett.*, 1981, **82**, 1–4.

26 K. Glänzer, M. Maier and J. Troe, Shock-Wave Study of the High-Temperature UV Absorption and the Recombination of CF_3 Radicals, *J. Phys. Chem.*, 1980, **84**, 1681–1686.

27 C. J. Cobos, A. E. Croce, K. Luther, L. Sölter, E. Tellbach and J. Troe, Experimental and Modeling Study of the Reaction $C_2F_4(+M)$ ↔ CF_2 + $CF_2(+M)$, *J. Phys. Chem. A*, 2013, **117**, 11420–11429.

28 C. J. Cobos, G. Knight, L. Sölter, E. Tellbach and J. Troe, Experimental and Modeling Study of the Multichannel Thermal Decomposition of CH_3F and CH_2F, *Phys. Chem. Chem. Phys.*, 2018, **20**, 2627–2636.

29 C. J. Cobos, L. Sölter, E. Tellbach and J. Troe, Shock Wave Study of the Thermal Dissociations of C_3F_6 and c-C_3F_6. II. Dissociation of Hexafluorocyclopropane and Dimerization of CF_2, *J. Phys. Chem. A*, 2014, **118**, 4873–4879.

30 C. J. Cobos, A. E. Croce, K. Luther and J. Troe, Temperature and Pressure Dependence of the Reaction 2 $CF_3(+M)$ ↔ $C_2F_6(+M)$, *J. Phys. Chem. A*, 2010, **114**, 4748–4754.

31 C. J. Cobos, A. E. Croce, K. Luther and J. Troe, Experimental and Modelling Study of the Unimolecular Thermal Dissociation of CHF_3, *Z. Phys. Chem.*, 2011, **225**, 1019–1028.

32 C. J. Cobos, A. E. Croce, K. Luther and J. Troe, Shock Wave Study of the Thermal Decomposition of CF_3 and CF_2 Radicals, *J. Phys. Chem. A*, 2010, **114**, 4755–4761.

33 C. J. Cobos, G. Knight, L. Sölter, E. Tellbach and J. Troe, Falloff Curves of the Reaction $CF_3(+M)$ → CF_2 + F(+M), *J. Phys. Chem. A*, 2020, **124**(7), 1235–1239.

34 G. Knight, L. Sölter, E. Tellbach and J. Troe, Shock Wave and Modeling Study of the Reaction $CF_4(+M)$ ↔ CF_3 + F(+M), *Phys. Chem. Chem. Phys.*, 2016, **18**, 17592–17596.

35 R. N. Hazeldine, Studies in Spectroscopy. Part III. the Ultra-violet Absorption Spectra of Halogen-containing aliphatic Iodo-compounds, and the Relative Stability of Free Halogen-containing Alkyl Radicals, *J. Chem. Soc.*, 1953, 1764–1771.

36 L. Zhang, W. Fuss and K. L. Kompa, Bond-Selective Photodissociation of CX (X = Br, I) in $XC_2H_4C_2F_4X$, *Chem. Phys.*, 1990, **144**, 289–297.

37 A. I. Maergoiz, E. E. Nikitin, J. Troe and V. G. Ushakov, Classical Trajectory and Statistical Adiabatic Channel

Study of the Dynamics of Capture and Unimolecular Bond Fission. V. Valence Interactions between Atoms and Linear Rotors, *J. Chem. Phys.*, 1998, **108**, 9987–9998.

38 C. J. Cobos and J. Troe, Theory of Thermal Unimolecular Reactions at High Pressures. II. Analysis of Experimental Results, *J. Chem. Phys.*, 1985, **83**, 1010–1015.

39 J. Troe, Predictive Possibilities of Unimolecular Rate Theory, *J. Phys. Chem.*, 1979, **83**, 114–126.

40 J. Troe and V. G. Ushakov, Revisiting Falloff Curves of Thermal Unimolecular Reactions, *J. Chem. Phys.*, 2011, **135**(054304), 1–10.

41 J. Troe and V. G. Ushakov, Representation of ''Broad'' Falloff Curves for Dissociation and Recombination Reactions, *Z. Phys. Chem.*, 2014, **228**, 1–10.

42 J. Troe, Theory of Thermal Unimolecular Reactions in the Falloff Range. I. Strong Collision Rate Constants, *Ber. Bunsenges. Phys. Chem*, 1983, **87**, 161–169.

43 N. Herath and A. G. Suits, Roaming Radical Reactions, *J. Phys. Chem. Lett.*, 2011, **2**, 642–647.

44 J. M. Bowman and B. C. Shepler, Roaming Radicals, *Annu. Rev. Phys. Chem.*, 2011, **62**, 531–553.

45 B. Joalland, Y. Shi, A. Kamasah, A. G. Suits and A. M. Mebel, Roaming Dynamics in Radical Addition-Elimination Reactions, *Nat. Commun.*, 2014, **5**(4064), 1–6.

46 E.-C. Wu and R. S. Rodgers, Kinetics of the Gas Phase Reaction of Pentafluoroethyl iodide with Hydrogen Iodide. Enthalpy of Formation of the Pentafluoroethyl Radical and the π Bond Dissociation Energy in Tetrafluoroethylene, *J. Am. Chem. Soc.*, 1976, **98**, 6112–6115.